Published in final edited form as:
Nat Photonics. 2021 July ; 15(7): 493–498. doi:10.1038/s41566-021-00791-1.

Multispectral Graphene-Based Electro-Optical Surfaces with Reversible Tunability from Visible to Microwave Wavelengths

M. Said Ergoktas[1,2], **Gokhan Bakan**[1,2], **Evgeniya Kovalska**[3], **Lewis W. Le Fevre**[2,4,5], **Richard P. Fields**[2], **Pietro Steiner**[1,2], **Xiaoxiao Yu**[1,2], **Omer Salihoglu**[3], **Sinan Balci**[6], **Vladimir I. Fal'ko**[2,7,8], **Kostya Novoselov**[2,7], **Robert A. W. Dryfe**[2,4,8], **Coskun Kocabas**[1,2,8,*]

[1]Department of Materials, University of Manchester, Manchester, M13 9PL, UK

[2]National Graphene Institute, University of Manchester, Manchester, M13 9PL, UK

[3]Department of Physics, Bilkent University, Ankara, Turkey

[4]Department of Chemistry, University of Manchester, Manchester, M13 9PL, UK

[5]Department of Electrical and Electronic Engineering, University of Manchester, Manchester, M13 9PL, UK

[6]Department of Photonics, Izmir Institute of Technology, Izmir, Turkey

[7]Department of Physics and Astronomy, University of Manchester, Manchester, M13 9PL, UK

[8]Henry Royce Institute for Advanced Materials, University of Manchester, Manchester, M13 9PL, UK

Abstract

Optical materials with colour-changing abilities have been explored for display devices[1], smart windows[2,3], or modulation of visual appearance[4–6]. The efficiency of these materials, however, has strong wavelength dependence, which limits their functionality to a specific spectral range. Here, we report graphene-based electro-optical devices with unprecedented optical tunability covering the entire electromagnetic spectrum from the visible to microwave. We achieve this non-volatile and reversible tunability by electro-intercalation of lithium into graphene layers in an optically accessible device structure. This unique colour-changing capability, together with area-selective intercalation, inspires fabrication of new multispectral devices, including display devices and electro-optical camouflage coating. We anticipate that these results provide realistic approaches for programmable smart optical surfaces with a potential utility in many scientific and engineering fields such as active plasmonics and adaptive thermal management.

* coskun.kocabas@manchester.ac.uk.

Author contributions: C.K. conceived the idea. M.S.E. synthesized the graphene samples and fabricated the devices. M.S.E., G.B., E.K., O.S., S.B., and C.K. performed the experiments. L.F., R.F., P.S., and X.Y. helped with the fabrication of the devices. V.F., K.N., and R.D. assisted with data analysis and manuscript preparation. G.B., M.S.E., and C.K. analysed the data and wrote the manuscript with input from all the authors. All authors discussed the results and contributed to the scientific interpretation as well as to the writing of the manuscript.

Additional information: C.K. is involved activities towards commercialization of graphene based optical surfaces under SmartIR Ltd. The work is subject to patent application by C.K., M.S.E., and G.B. The remaining authors declare no competing financial interests.

Europe PMC Funders Author Manuscripts

Conventional optoelectronic devices, e.g., light sources and detectors, are intentionally designed to operate at a certain wavelength range to obtain the highest efficiency. There might be new opportunities for optoelectronic devices that can operate over seemingly unrelated wavelengths such as the visible and terahertz (THz) light whose energies differ by three orders of magnitude. Applications that could exploit these multispectral operations include, for example, adaptive camouflage coatings that can perform concealment both in the visible and infrared wavelengths, a display device that can encode information in different wavelengths or a dynamic thermal blanket that can selectively reflect visible or infrared light. Such multispectral devices could be possible, if they can overcome existing challenges of requiring (1) broadband electro-optical tunability, (2) multispectral device structure, and (3) non-volatile switching. The research on tunable optical materials has primarily focused on controlling the state of materials to alter the optical response. Phase-change[7–9] and electrochromic[10,11] materials are two examples that are capable of colour change triggered by temperature change or electric field. The existing device structures such as the requirement of a conductive top electrode limit their spectral operation range and utility for a multispectral application.[12,13]

Electro-intercalation of atomic or molecular ions into layered materials, such as graphite intercalation compounds (GICs), can rise to the challenge by providing the host material new means of controlling its electrical, optical, thermal, and magnetic properties.[14–17] Tuning optical properties of the host material *via* intercalation, however, has been overlooked mainly due to the difficulties of integration of optical devices with electrochemical cells.[17,18] In this Letter, we report an electrochemical optical platform with non-volatile and reversible reflectivity modulation covering the entire electromagnetic spectrum from the visible to microwave regime. This platform differs from previously reported graphene devices, which are designed primarily for specific wavelength ranges of microwave,[19] THz,[20] infrared,[5,6] and visible[21] using single and multilayer graphene. Overcoming the challenge of extending the coverage to the visible while keeping the optical activity at the longer wavelengths has led to the innovative device structure reported here to reach the ultimate multispectral operation.

Figure 1a illustrates the structure of the device and its operation principle. The device takes advantage of multilayer graphene (MLG, ~150 layers) as the anode and as well as the optically active material. The number of graphene layers is estimated using visible-NIR transmission measurements and optical modelling (See Supplementary Note 1, Figure S1). High electrical conductivity of MLG (<50 Ω/sq) eliminates the requirement of an additional top electrode layer. The key feature of the device is that MLG is optically accessible under a transparent protection layer. This is achieved by laminating MLG and vacuum sealing the device in a low-density polyethylene pouch (LDPE, 0.91-0.94 g/cm^3 density and crystallinity of 42-62%) that has over 90% optical transparency from the visible to microwave wavelengths, except for the infrared absorptions in the fingerprint region (Figure S2). The airtight packaging is crucial for a stable non-volatile operation. Aluminium foil, coated with lithium-doped nickel manganese cobalt oxide (NMC), is used as the cathode and the source of Li^+ ions. Electro-intercalation of Li^+ ions into MLG (charging the device) is achieved by applying a constant electric current (~1 mA/cm^2) towards the cathode (Figure

1b). The device voltage was monitored to track the state of charge (SoC). Reversing the current direction, or simply shorting through an electrical load (Figure S3 and Video S1), de-intercalates the ions from MLG, making the operation reversible and repeatable.[22] During intercalation (or de-intercalation), the optical properties of MLG change drastically. Discharged device appears dark grey owing to the high absorptivity (>80%) of the top graphene layer in the visible regime. When the device is fully charged (at ~3.8 V), the graphene layer appears gold in colour (Figure 1c), similar to stage 1 GIC.[16,23] The achievable colour space can be enriched to include a range from red to blue using optical effects such as thin-film interference (See Supplementary Note 2 and Figure S4-S5). This can further lead to generation of arbitrary colours using subpixels and varying the optical reflectivity with SoC in a similar way employed by display devices. Besides the visible colour change, the infrared properties follow a similar trend and exhibit low reflectivity (R ~30%), hence high emissivity (ε ~0.7), when discharged and high reflectivity (R ~75%), hence low emissivity (ε ~0.25) when charged (Figure 1d). Thermal imaging of the device was performed outdoors to minimize the ambient thermal emission reflected from the device. The charged device appears significantly colder (<5 °C) to the thermal camera compared to its actual temperature owing to its low infrared emissivity. The device operation resembles that of Li-ion batteries with Coulombic efficiency over 85% for more than 2200 charge/discharge cycles (Figure S6).

To examine the multispectral response, we measured the reflection spectra of the devices at different doping levels. By combining the reflection measurements from three different spectrometers (Ultraviolet/Visible/Near-infrared, Fourier Transform Infrared (FTIR) Spectrometer, and Time-domain THz Spectrometer), we obtained the reflectivity change from the ultraviolet (λ=300 nm) to microwave (λ=3 mm) as shown in Figure 2a. The reflectivity can be modulated in the entire range of the non-ionising part of the electromagnetic spectrum. Figure 2b compares the reflectivity modulation for three sample wavelengths from the visible (λ=500 nm), infrared (λ=10 μm), and THz (λ=1 mm) regimes. The modulation onset varies with the wavelength of light. The THz reflectivity increases at the state of charge of ~0.05 whereas the modulation in the infrared and visible regime starts appearing at ~0.2 and ~0.4 SoC, respectively. The sharp drop in the reflectance is an indicator of the free-carrier plasma resonance ω_p. This reflection minima shifts from the far-infrared to ultraviolet for increasing doping. The experimental spectra can be modelled using intraband (Drude) and interband optical conductivity: $\varepsilon = \varepsilon_\infty + \varepsilon_{int} + i\frac{\omega_p^2 \tau}{\omega(1 - i\omega\tau)}$,, ε_∞ where is the background dielectric constant, ε_{int} accounts for the contribution of interband transitions, τ is the scattering time of carriers, and ω is the angular frequency of light (see Supplementary Note 3 and Figure S7). Fitting the model to the reflectivity measurements shows that the plasma frequency varies from 0.1 to 9 eV (Figure 2c) and the scattering time from 30 to 1 fs with charging (Figure S8). At higher doping levels, stage-1 and stage-2 intercalated graphitic compounds show significantly smaller scattering time (10 – 20 fs) due to additional scattering from charged intercalate ions and electron-electron scattering.[24] For the same device structure, Figure 2d shows the variation in the sheet resistance of MLG and the device voltage during charging cycle. Clear steps are observed in these measurements indicating the distinct intercalation stages.

For more insights into the intercalation process, we performed *in-situ* Raman and photoluminescence measurements (with 633 nm and 457 nm excitations) during charging and discharging cycles (See Supplementary Note 4 for the complete Raman analysis). Figure 3a-c illustrate doping-induced change in possible Raman pathways for the G and 2D-bands. As we charge the device, Raman G-band at 1581 cm^{-1}first shifts to 1590 cm^{-1} due to the Kohn anomaly[25–27] and splits into two peaks[28] then disappears due to the Pauli blocking[29] of Raman pathways. Similarly, the intensity of 2D-band decreases gradually and disappears at relatively lower voltages (~3.48 V) (Figure 3d). We also observed hot luminescence from heavily doped MLG at energies < $2E_F$, where excited-state relaxation pathways become available. The hot luminescence also disappears due to the Pauli blocking of the laser excitation (Figure 3e). We extract the Fermi energy, E_F (Figure 3f) using the onset and cut-off of the hot luminescence, the Pauli blocking condition for G-band $2E_F = E_{ex}$ and for 2D-band $2E_F = E_{ex} - \hbar\Omega_D$, where E_{ex} is the excitation energy and Ω_D is the energy of the D-band phonons. These results are in good agreement with the Fermi energy extracted from optical transmission measurements (Figure 3f). Our results show that the Fermi energy of MLG can be reversibly increased up to 1.5 eV which is consistent with the band structure calculations of LiC_6.[30] Raman analysis also shows that the graphene layer stays intact even after 20000 intercalation/deintercalation cycles suggesting that the degradation of the devices is not due to structural damages to the graphene layer but instead due to the loss of Li-ions on the cathode electrode (Figure S19).

To show the promises of the tunable multispectral optical surfaces, we demonstrate two proof-of-concept (PoC) devices. The first device is a display capable of showing images in the visible, infrared, and THz wavelengths, simultaneously. Figure 4a shows cross-section illustration of the device, which uses continuous graphene layer and area-selective intercalation of Li^+ ions enabled by patterning the cathode. Controlling the voltage applied to an individual electrode enables varying the pixel's spectral response. Figure 4b showcases the display device with its back electrode patterned into letters "N", "G", and "I" (the initials of National Graphene Institute). Multispectral imaging of the device was performed by a CMOS camera operating in the visible regime (400 – 700 nm), a long-wave infrared camera (8 – 13 μm), and THz raster-scan imaging system (0.5 – 2 THz). Applying 3.8, 3.5, and 3.3 V to "N", "G", and "I" pixels, respectively, revealed "N" in all wavelengths, "G" in the infrared and THz, and "I" only in the THz. Such an example is first of its kind and, beyond the demonstrated function as a multispectral display, it has the potential to be used for optical security applications in which an encoded message can only be revealed with the correct key that corresponds to applying a specific voltage to the device and imaging in a specific range of wavelengths for our technology. The demonstrated concept relies on non-overlapping voltage ranges for different spectral regimes, e.g., being able to change the infrared emission while maintaining the visible response. This feature is visualized on a device by (i) changing both the visible and infrared response, (ii) changing only the infrared response while the visible reflection is always low, and (iii) changing only the visible response while the infrared emission is always low (Video S2). The devices leverage flexible printed circuit board technology to build flexible, multipixel, and multispectral displays (Figure S22).

The second PoC device is a multispectral adaptive camouflage system that has a unique capability of modifying its visible and infrared appearance dynamically. The adaptive visibility was achieved by patterning the back electrode into a camouflage pattern. Then, specific parts of the device were activated to match its appearance to that of a spatially varying background (Figure 4c). The graph in Figure 4c shows time trace of the red, green, and blue (RGB) colour indices during adaptation. Adaptation capabilities of these optical surfaces can be improved by integrating pixelated devices with visual feedback. Similarly, the device can adapt its thermal appearance. Figure 4d, e shows thermal images of a device as it adapts its infrared emission to cold and hot backgrounds (see Video S3). These demonstrations highlight a comprehensive case of thermal camouflage where the background infrared emission dynamically changes taking into account moving targets and changing environmental factors, e.g., ambient temperature, clouds (see Supplementary Note 5 for further discussions). While the background in these examples was kept spatially uniform, we demonstrated that the approach used for the visible camouflage can be adapted for a spatially varying thermal background (Figure S23). The time-trace of the infrared camouflage process reveals the high transition speed (~1 s) and quantifies how well the infrared emission from the device (rendered as the apparent temperature by the camera) adapts to the background (shaded areas in Figure 4d, e). The camouflage operation can easily be extended into the mid-wave (3 – 5 μm) and short-wave (1.4 – 3 μm) infrared regimes as the emissivity modulation covers the entire infrared spectrum (Figure S24). We performed benchmarking studies of our devices against existing thermal metamaterials and other variable-emissivity technologies. The key device metrics for cloaking applications are tuning mechanism, response time, and power consumption. (Supplementary Note 6 and Table S2).

In the final part, we discuss how the multispectral tunability can improve adaptive thermal management of satellites in outer space by balancing the absorbed solar radiation (wavelength range: 0.3 – 2.5 μm) and the internal heat generated by satellite electronics with the emitted infrared radiation (peaks ~10 μm) (Figure 5a-c). Maintaining this balance with passive optical components while the satellite orbits the earth creates major design challenges especially for small satellites.[31] The demonstrated multispectral electro-optical tunability in the visible and infrared regimes can address this need by varying the visible absorptivity and infrared emissivity with the state of charge (Figure 5d). For the calculations, we used a low orbit (altitude of 600 km) CubeSat as a model system for two extreme cases: (i) when the satellite is exposed to direct sunlight, (ii) in earth's shadow. For the first case, rejecting the incident solar irradiance is the priority as the solar irradiance at the satellite's orbit (~1347 W/m^2) is much larger than a blackbody at 30 °C can emit to the deep space (~479 W/m^2). Varying the state of charge on surfaces that are not exposed to sunlight provides a dynamic net cooling rate as large as 141 W/m^2. For the second case, all sides but the earth-facing one are exposed to the deep space and the satellite receives no direct or indirect solar radiation. The net cooling rate in this case is evaluated between 95 and 282 W/m^2 with varying state of charge (Figure 5d). In contrast, a thermal coating with static optical properties can only provide a static cooling rate making the satellite prone to larger temperature fluctuations with varying satellite position and activity ($\Delta T \approx 6$ °C for static vs. 0 °C for our coating, see Supplementary Note 7 for a detailed analysis).

The temporal response of the device is of critical importance for these applications. The switching speed is limited by the intercalation process, quantified as the state of charge in this work that has linear dependence on the device current. For a moderate current density of ~1 mA/cm^2, full charging and accompanying optical changes take place in ~40 s being superior to the electrochromic alternatives operating in the visible regime with switching durations ranging from tens of seconds to minutes.[10] Switching the THz and infrared response is faster in comparison with a response time on the order of 1 s and a few seconds, respectively (see Supplementary Note 8, Figure S26).

The long-term steady operation of the devices necessitates maintaining the initial purity of the electrolytes, specifically the low moisture (<15 ppm) and HF (<50 ppm) contents. The same problem present for Li-ion batteries is solved by airtight packing and solid-electrolyte interface.[32] Following this example, our devices were vacuum sealed in polyethylene pouches to press all layers against each other while keeping the graphene layers optically accessible. The endurance of the devices was tested in the THz, infrared, and visible regimes. The results show that devices can operate more than 11000, 2200, and 580 on/off cycles in these regimes, respectively (see Figure S27-S28-S29 and Supplementary Note 9). Thanks to the recent advances of graphene growth, we anticipate that these devices are compatible for large-scale production (Figure S30). Beyond the PoC demonstrations included here, the developed technology inspires new applications such as battery level indicator for Li-ion batteries (Figure S31).

In conclusion, we demonstrate multispectral electro-optical devices operating over the entire electromagnetic spectrum from the visible to microwave. This unprecedented capability would inspire new technologies that has a very high potential to reshape the tunable optics either as a standalone unit or by incorporating with established light manipulation approaches. Furthermore, the demonstrated broad electro-optical tunability of the plasma frequency yields a unique electrically tunable plasmonic system which would enable multispectral active plasmonics.

Materials and Methods

MLG Synthesis

MLG was synthesized by CVD (planarTECH CVD) on 25-μm-thick nickel foils (Alfa Aesar, 12722). First, nickel foil substrate was heated to the growth temperature of 1050 °C under 100 sccm H_2, and 100 sccm Ar flow and annealed at 1050 °C for 20 minutes. Then, 35 sccm CH_4flow was used as carbon precursor for 15 minutes at atmospheric pressure with addition to 100 sccm H_2, and 100 sccm Ar flow at 1050 °C. Lastly, the sample was cooled down to the room temperature quickly under 100 sccm H_2 and 100 sccm Ar flow. Thickness of the MLG is ~150 layers.

MLG Transfer

20-μm-thick polyethylene was laminated on MLG on Ni foil at 160 °C. Ni was etched in 1M $FeCl_3$ solution in ~8 hours and rinsed with DI water.

Device Fabrication

Li-NMC (LiNiMNCoO2, 5:3:2) coated Al foil was used as cathode. 25-μm-thick, porous polyethylene membrane placed on top of NMC layer as a separator. A frame of Cu foil was placed on the porous polyethylene to function as an electrode for MLG. MLG transferred on polyethylene was placed on top of the separator as MLG facing down and in contact with the Cu frame. Battery grade $LiPF_6$ in EC/DEC 1:1 (Lithium hexafluorophosphate in ethylene carbonate and diethyl carbonate from Gelon Energy Co., Ltd.) applied to the separator (~250 μl for 3×3 cm^2 area). The device was placed in a polyethylene pouch and vacuum sealed. For the multispectral display device, Li-NMC-coated Al foil was patterned with a plotter to electrically isolate the pieces from each other. For the sheet resistance measurements, in addition to above procedure, we placed 4 additional copper contacts on the corners of the MLG for the van der Pauw technique.

Spectroscopic characterization

Visible and NIR reflection measurements were performed with Cary 5000 UV-VIS-NIR spectrometer equipped with an integrating sphere. Infrared images and videos were recorded with a FLIR T660 thermal camera. Infrared reflection measurements were carried out using a Perkin Elmer Spectrum 100 FTIR spectrometer equipped with Mid-IR integrating sphere (PIKE Mid-IR IntegratIR) and a wide band liquid-nitrogen-cooled mercury-cadmium-telluride detector at a spectral resolution of 4 cm^{-1}. The emissivity, ε, values were calculated from the measured reflection, R, spectra: $\varepsilon = 1 - R$. THz reflection measurements were performed using time domain THz spectrometer (Toptica Teraflash) which uses two InGaAs photoconductive antennas as THz transmitter and receiver. THz pulse was guided using a reflection head, which contains 4 parabolic mirrors to focus the THz pulse onto a sample and focus the reflected THz pulse back to the receiver antenna. Raman measurements were performed using a Renishaw inVia Raman Spectrometer equipped with 457, 488, 514, 633 nm lasers and 50x objective. For the sheet resistance measurements, two Keithley 2400 source meters were used: one for charging the device and the other for the 4-point resistance measurement. Before charging the device, its sheet resistance was measured following the standard van der Pauw method. Then, the 4-point resistance of the device was measured at 5 s intervals for the charging cycle. Charging was interrupted while measuring the device resistance to avoid measurements flawed by the source meter charging the device. The change in the 4-point device resistance and the initial sheet resistance were used to evaluate the curve seen in Figure 2c.

Supplementary Material

Refer to Web version on PubMed Central for supplementary material.

Acknowledgements

This research is supported by European Research Council through ERC-Consolidator Grant (grant no 682723, SmartGraphene) and ERC-PoC Grant (grant no 899908, SmartIR). In addition, we acknowledge Graphene Engineering Innovation Centre (GEIC) for access to the CVD system.

Data availability

Data is available on request from the authors.

Code availability

The custom code used for fitting of optical reflectivity is available on request from the authors.

References

1. Hosseini P, Wright CD, Bhaskaran H. An optoelectronic framework enabled by low-dimensional phase-change films. Nature. 2014; 511:206–211. [PubMed: 25008527]
2. Lin J, et al. Thermochromic halide perovskite solar cells. Nat Mater. 2018; 17:261–267. [PubMed: 29358645]
3. Montelongo Y, et al. Electrotunable nanoplasmonic liquid mirror. Nat Mater. 2017; 16:1127–1135. [PubMed: 28892055]
4. Yu C, et al. Adaptive optoelectronic camouflage systems with designs inspired by cephalopod skins. Proc Natl Acad Sci U S A. 2014; doi: 10.1073/pnas.1410494111
5. Salihoglu O, et al. Graphene-Based Adaptive Thermal Camouflage. Nano Lett. 2018; 18:4541–4548. [PubMed: 29947216]
6. Ergoktas MS, et al. Graphene-Enabled Adaptive Infrared Textiles. Nano Lett. 2020; 20:5346–5352. [PubMed: 32551694]
7. Wuttig M, Bhaskaran H, Taubner T. Phase-change materials for non-volatile photonic applications. Nature Photonics. 2017; doi: 10.1038/nphoton.2017.126
8. Zhang Y, et al. Broadband transparent optical phase change materials for high-performance nonvolatile photonics. Nat Commun. 2019; 10:1–9. [PubMed: 30602773]
9. Bakan G, Ayas S, Saidzoda T, Celebi K, Dana A. Ultrathin phase-change coatings on metals for electrothermally tunable colors. Appl Phys Lett. 2016; 109
10. Granqvist CG, et al. Electrochromic materials and devices for energy efficiency and human comfort in buildings: A critical review. Electrochim Acta. 2018; 259:1170–1182.
11. Lu N, et al. Electric-field control of tri-state phase transformation with a selective dual-ion switch. Nature. 2017; 546:124–128. [PubMed: 28569818]
12. Llordés A, Garcia G, Gazquez J, Milliron DJ. Tunable near-infrared and visible-light transmittance in nanocrystal-in-glass composites. Nature. 2013; 500:323–326. [PubMed: 23955232]
13. Runnerstrom EL, Llordés A, Lounis SD, Milliron DJ. Nanostructured electrochromic smart windows: traditional materials and NIR-selective plasmonic nanocrystals. Chem Commun. 2014; 50:10555–10572.
14. Daukiya L, et al. Functionalization of 2D materials by intercalation. Prog Surf Sci. 2019; 94:1–20.
15. Wan J, et al. Tuning two-dimensional nanomaterials by intercalation: Materials, properties and applications. Chem Soc Rev. 2016; 45:6742–6765. [PubMed: 27704060]
16. Dresselhaus MS, Dresselhaus G. Intercalation compounds of graphite. Adv Phys. 1981; 30:139–326.
17. Bao W, et al. Approaching the limits of transparency and conductivity in graphitic materials through lithium intercalation. Nat Commun. 2014; 5:1–9.
18. Pfluger P, Künzi HU, Güntherodt H. Discovery of a new reversible electrochromic effect. Appl Phys Lett. 1979; 35:771–772.
19. Balci O, Polat EO, Kakenov N, Kocabas C. Graphene-enabled electrically switchable radar-absorbing surfaces. Nat Commun. 2015; 6:6628. [PubMed: 25791719]
20. Kakenov N, et al. Observation of Gate-Tunable Coherent Perfect Absorption of Terahertz Radiation in Graphene. ACS Photonics. 2016; 3:1531–1535.
21. Polat EO, et al. Graphene-Enabled Optoelectronics on Paper. ACS Photonics. 2016; 3:964–971.

22. Xiao J, et al. Understanding and applying coulombic efficiency in lithium metal batteries. Nat Energy. 2020; doi: 10.1038/s41560-020-0648-z
23. Lodico JJ, et al. Irreversibility at macromolecular scales in the flake graphite of the lithium-ion battery anode. J Power Sources. 2019; 436
24. Brida D, et al. Ultrafast collinear scattering and carrier multiplication in graphene. Nat Commun. 2013; 4:1–9.
25. Piscanec S, Lazzeri M, Mauri F, Ferrari AC, Robertson J. Kohn anomalies and electron-phonon interactions in graphite. Phys Rev Lett. 2004; 93
26. Pisana S, et al. Breakdown of the adiabatic Born-Oppenheimer approximation in graphene. Nat Mater. 2007; 6:198–201. [PubMed: 17293849]
27. Das A, et al. Monitoring dopants by Raman scattering in an electrochemically top-gated graphene transistor. Nat Nanotechnol. 2008; 3:210–215. [PubMed: 18654505]
28. Sole C, Drewett NE, Hardwick LJ. Insitu Raman study of lithium-ion intercalation into microcrystalline graphite. Faraday Discuss. 2014; 172:223–237. [PubMed: 25427224]
29. Zhao SYF, et al. Controlled Electrochemical Intercalation of Graphene/h-BN van der Waals Heterostructures. Nano Lett. 2018; 18:460–466. [PubMed: 29268017]
30. Echeverry JP, Chulkov EV, Echenique PM, Silkin VM. Low-energy collective electronic excitations in LiC6,SrC6, and BaC6. Phys Rev B. 2019; 100
31. Osiander R, Firebaugh SL, Champion JL, Farrar D, Darrin MAG. Microelectromechanical devices for satellite thermal control. IEEE Sens J. 2004; 4:525–531.
32. Jansen AN, Amine K, Henriksen GL. Low-cost flexible packaging for high-power Li-Ion HEV batteries. Anl-04/09. 2004; doi: 10.2172/828774

Europe PMC Funders Author Manuscripts

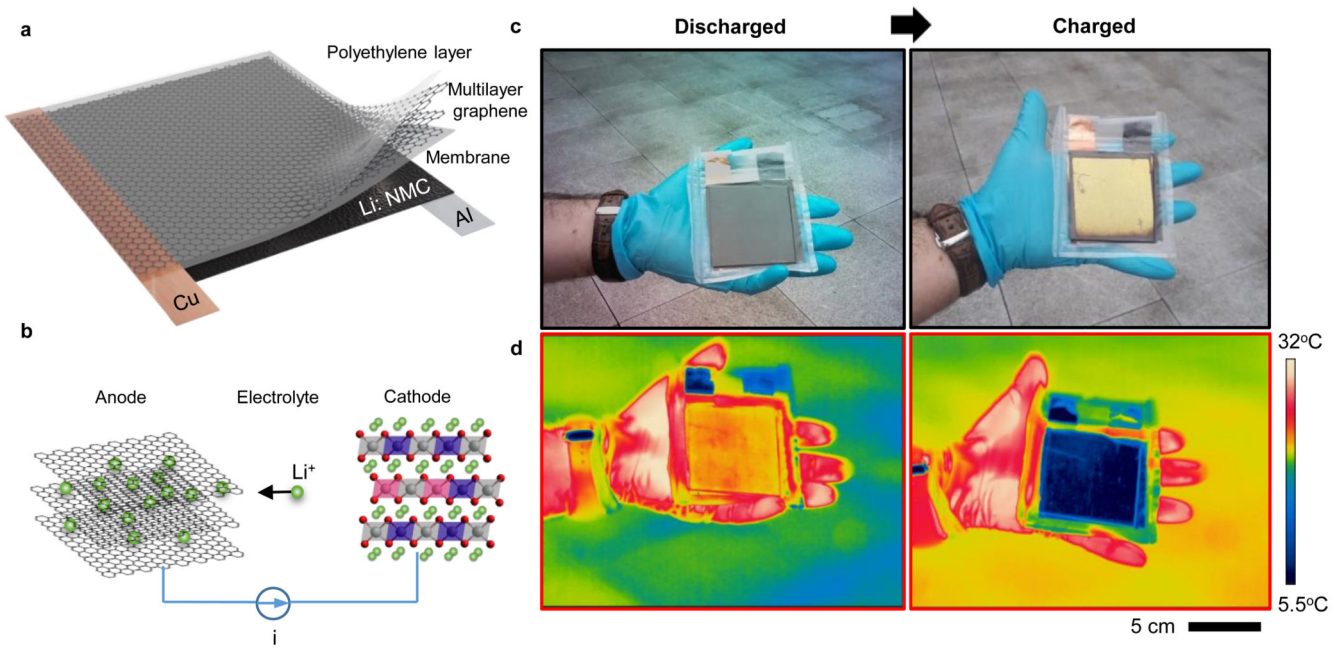

Figure 1. Device structure and operation principle.

a, Schematic drawing of the device consisting of polyethylene protection, multilayer graphene (anode), electrolyte-containing membrane, and aluminium foil coated with lithium-doped Ni-Mn-Co-oxide (cathode). **b**, Illustration of Li^+ ion intercalation into graphene layers. **c**, Visible and **d**, Infrared images of the device at fully discharged and charged states showing non-volatile multispectral tunability.

Europe PMC Funders Author Manuscripts

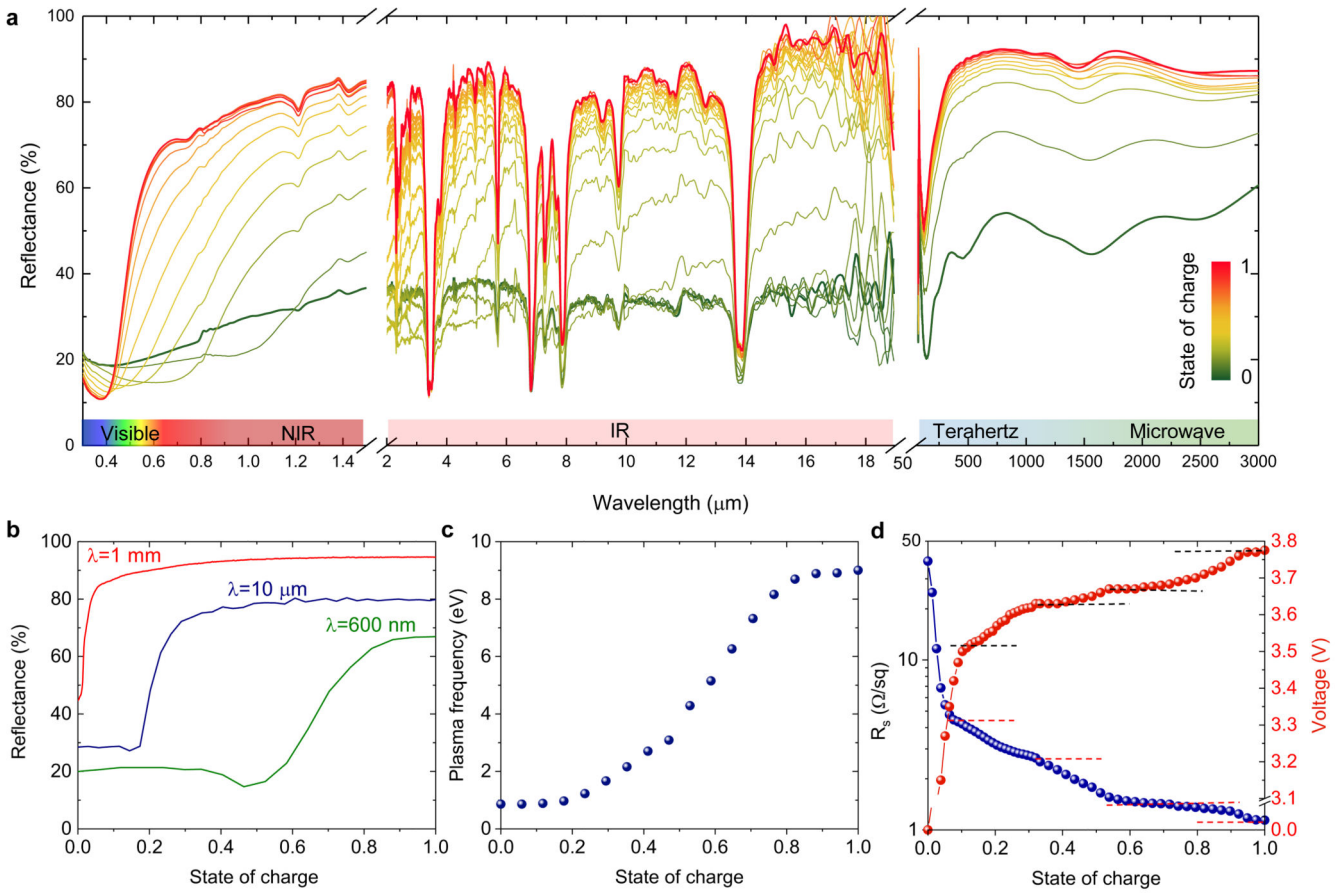

Figure 2. Multispectral tunability from visible to microwave.

a, Measured reflection spectra covering the visible, infrared, THz, and microwave regimes for different doping levels (state of charge). The general trend is increasing reflectance with increasing state of charge. The sharp reflection dips in the infrared spectrum are due to absorption by the top polyethylene protection layer. **b**, Variation in the reflectivity of the device at the selected wavelengths of 600 nm, 10 μm, and 1 mm. **c**, Change in the plasma frequency as a function of the state of charge. **d**, Device voltage and sheet resistance of MLG during charging. Dashed lines mark the different stages of lithiation of graphene.

Europe PMC Funders Author Manuscripts

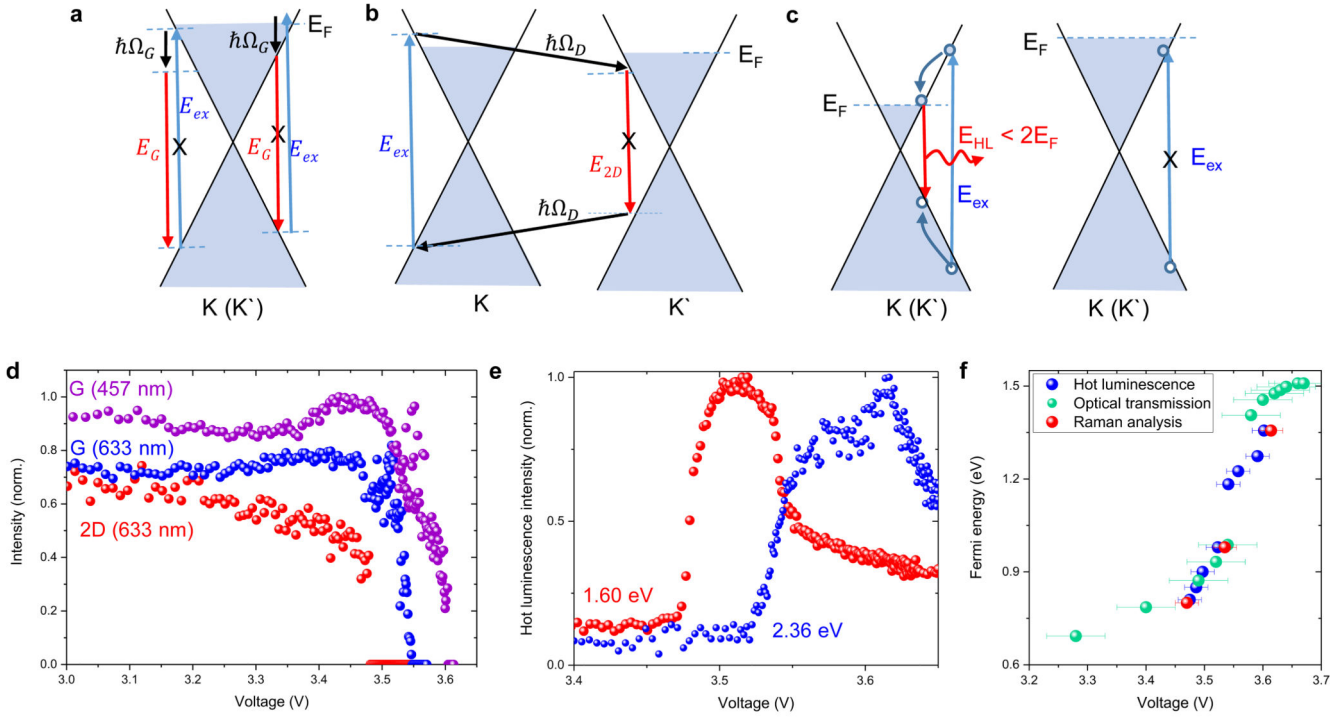

Figure 3. In situ Raman characterization of intercalation process

a-b Illustration of gate-induced change in possible Raman pathways for the G and 2D-bands. **c**, Illustration of hot electron photoluminescence pathways in doped MLG and its Pauli blocking condition. **d**, Variation of the Raman intensity of G and 2D peaks as a function of voltage. **e**, Voltage dependence of hot luminescence from MLG at energies of 1.60 and 2.36 eV. **c**, Voltage dependence of the Fermi energy of MLG extracted from the Pauli blocking conditions of the Raman peaks, hot luminescence, and optical transmission. The error bars indicate the uncertainty in obtaining the voltage values for the Pauli blocking condition.

Europe PMC Funders Author Manuscripts

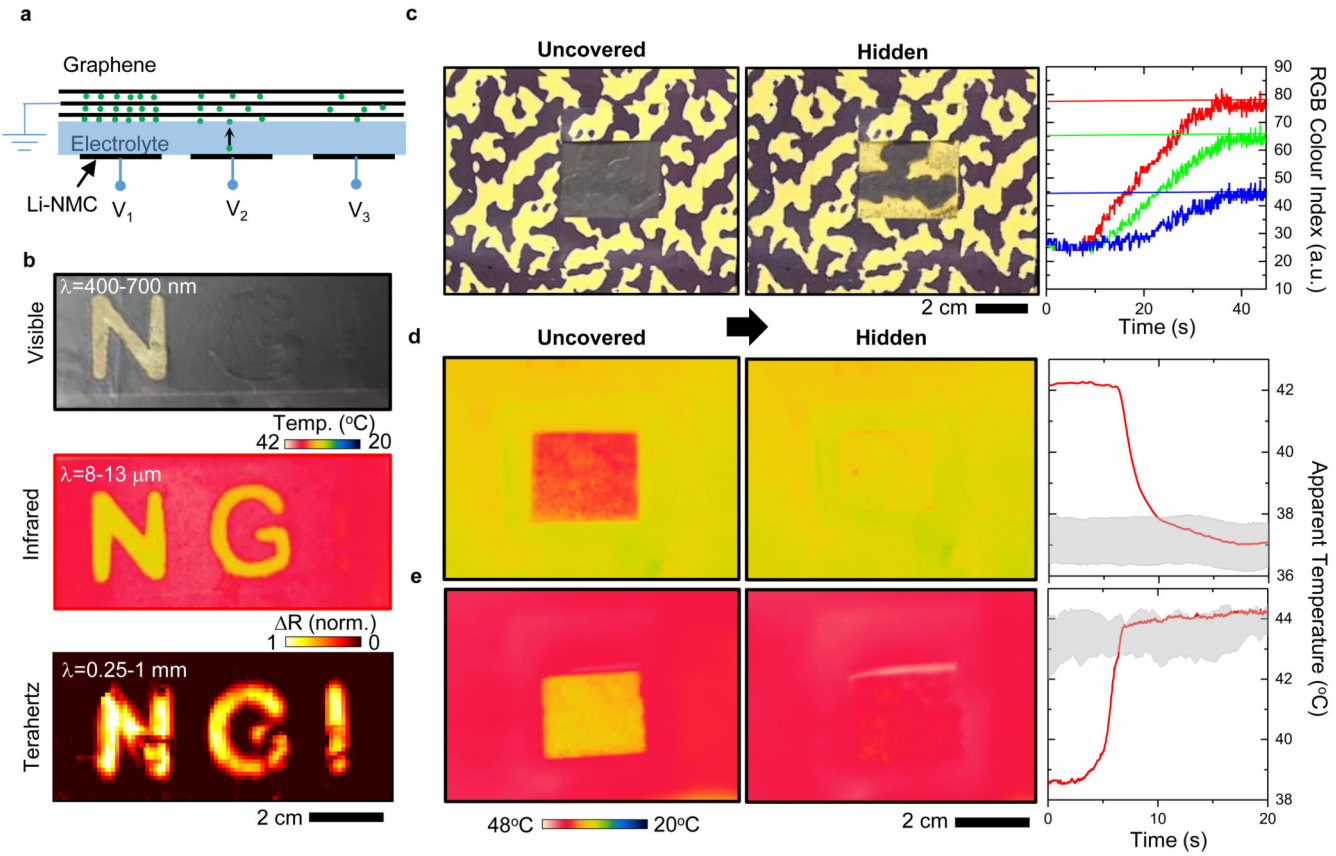

Figure 4. Multispectral display and adaptive camouflage.

a, Cross section illustration of PoC multispectral display based on area-selective lithiation. Patterned cathodes define individually addressable pixels. The state of charge determines the operation wavelength. **b**, Images of a display device rendered in the visible, infrared, and THz regimes. **c**, Demonstration of adaptive visible camouflage. The device blends into a spatially varying background by matching its visible appearance. The graph shows the change in red, green, and blue (RGB) colour indices from the active region of the device as it blends in. Vertical lines mark the background RGB indices. **d**, **e**, Demonstration of adaptive infrared camouflage. The device can adapt its infrared emission to blend in cold (d) and hot (e) backgrounds. Graphs show the time-trace of the apparent device temperature during adaptation. The shaded areas show the background temperature range.

Europe PMC Funders Author Manuscripts

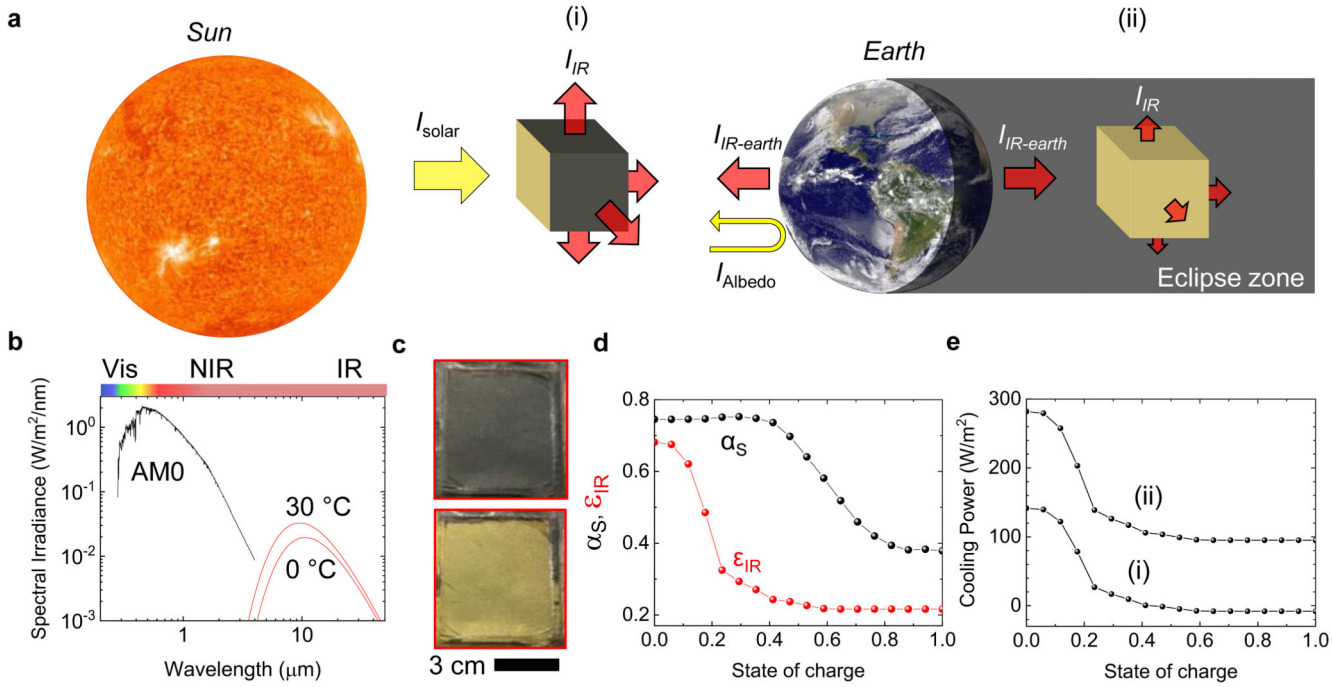

Figure 5. Adaptive thermal management for satellites.

a, Schematic drawing of a CubeSat orbiting the earth, illustrating the solar and infrared irradiance on it. (Sun and Earth images by NASA are licensed under CC BY 2.0) **b**, Spectral solar irradiance on a low-earth-orbiting satellite and blackbody radiation at 0 and 30 °C. **c**, Photographs of a large-area device at zero and full state of charge. This device can fully cover single side of a CubeSat. **d**, Weighted solar absorptivity and infrared emissivity of the developed multispectral surfaces as a function of state of charge. **e**, Calculated cooling power of the satellite (i) under direct sunlight and (ii) in earth's shadow.

Europe PMC Funders Author Manuscripts